

Demonstration of ultra-low emittance beams in a kHz laser wakefield accelerator and application to electron diffraction

J. Monzac,^{1,*} S. Smartsev,¹ J. Huijts,¹ A. Vernier,¹ I. A. Andriyash,¹ V. Tomkus,² V. Girdauskas,^{2,3} G. Raciukaitis,² M. Mackevičiūtė,² V. Stankevič,² A. Cavagna,¹ J. Kaur,¹ A. Kalouguine,¹ R. Lopez-Martens,¹ and J. Faure¹

¹*Laboratoire d'Optique Appliquée (LOA), CNRS, École polytechnique,*

ENSTA, Institut Polytechnique de Paris, Palaiseau, France

²*Center for Physical Sciences and Technology, Savanoriu Ave. 231, LT-02300, Vilnius, Lithuania*

³*Vytautas Magnus University, K. Donelaicio St. 58. LT-44248, Kaunas, Lithuania*

(Dated: February 16, 2026)

We present a compact, cost-effective method for measuring the emittance of kHz-repetition-rate laser-wakefield accelerated electron beams using a permanent solenoid. The measured normalized emittance, $\epsilon_n = 124 \text{ nm} \cdot \text{rad}$ ($\simeq 0.04\pi \text{ mm} \cdot \text{mrad}$) at 2.7 MeV, is comparable to that of ultra-low emittance radiofrequency guns used for electron diffraction. Leveraging this low emittance, we successfully applied the electron beam to electron diffraction. We demonstrate diffraction images obtained from a single crystal Silicon nano-membrane sample, clearly resolving diffraction peaks across multiple orders.

I. INTRODUCTION

Laser wakefield acceleration (LWFA) is a promising method for accelerating electrons to relativistic energies over very short distances using high-intensity laser pulses to drive plasma wakefield [1]. Modern LWFA systems, driven by 100 TW to PW lasers, routinely produce electron beams with energies ranging from a few MeV to several GeV within centimeters [2–8]. The MeV-scale electron beams accelerated via LWFA hold significant potential for Ultrafast Electron Diffraction (UED), a pump-probe technique that probes ultrafast structural dynamics in materials [9–11]. In UED, a laser pulse excites the material, and electron diffraction images are captured at varying time delays to observe its time-resolved response. The UED's temporal resolution is thus limited by the probe beam duration, space charge [11], and shot-to-shot jitter [12, 13]. LWFA beams, however, offer intrinsic advantages: femtosecond duration [14], high charge, and minimal shot-to-shot jitter (the accelerating structure is directly driven by the laser), and could enable sub-10-fs resolution [15]. For UED applications, these beams must display good shot-to-shot stability with high repetition rates, along with low emittance to ensure transverse coherence.

Recent advances have significantly improved the stability of LWFA beams. High-quality statistics have been demonstrated on a continuous 24 h experiment at 1 Hz in [16], and the continuous and stable operation of a kHz LPA for 5 hours using a free-flowing nitrogen jet has been demonstrated in [17]. Latest experiments confirmed the potential of LWFA for producing highly stable and well-defined low-energy electron beams at kHz, with beam-pointing fluctuations below 2.3 mrad RMS and charge fluctuations under 7% RMS [18].

The quality of a particle beam can be quantified using its emittance, which describes the volume it occupies in the 6D phase-space defined by spatial coordinates (x, y, z) and momenta (p_x, p_y, p_z). The transverse emittances are projections of the beam's phase-space distribution: for a beam propagating along z , the transverse normalized emittance along x is a projection onto the (x, p_x) plane:

$\epsilon_{n,x} = \frac{1}{m_e c} \sqrt{\langle x^2 \rangle \langle p_x^2 \rangle - \langle x p_x \rangle^2}$ with m_e the electron mass and c the speed of light. The transverse normalized emittance represents the beam's spatial quality and its ability to be tightly focused. In practice, experimental methods rather give access to the transverse geometric emittance $\epsilon_{g,x} = \sqrt{\langle x^2 \rangle \langle x'^2 \rangle - \langle x x' \rangle^2}$, a quantity defined in trace-space (x, x') where $x' = p_x/p_z$ is an angle. For a monochromatic beam, the geometric and normalized emittance are simply linked by: $\epsilon_{n,x} = \gamma \beta_z \epsilon_{g,x}$ where γ is the Lorentz factor and $\gamma \beta_z = p_z/m_e c$ the normalized longitudinal momentum, so that the normalized emittance can be easily retrieved from the measurement of the geometric emittance.

The normalized transverse emittance $\epsilon_{n,x}$ of the electron beam directly affects its transverse coherence length L_T . For a beam with small divergence, L_T at the sample position is given by [19]:

$$L_T = \frac{\hbar}{m_e c} \frac{\sigma_x}{\epsilon_{n,x}} \quad (1)$$

where σ_x is the size of the beam on the sample. However, L_T can also be expressed in terms of the experimental setup as $L_T = \frac{\lambda_B d}{a}$ where λ_B is the de Broglie wavelength associated to the electron beam, d the source-sample distance, and a the lattice parameter of the sample. To resolve interference when $a = 5 \text{ \AA}$ (similar to silicon), L_T must exceed 1 nm. For $\sigma_x = 200 \text{ \mu m}$, this imposes $\epsilon_{n,x} < 77 \text{ nm} \cdot \text{rad}$. Thus, achieving low-emittance beams is essential for high-quality UED.

Several methods exist to measure the emittance of

* josephine.monzac@laplace.univ-tlse.fr

an electron beam, many of which are detailed in [20]. However, measuring the emittance of electron beams generated by LWFA presents additional challenges due to the beams' shot-to-shot fluctuations and inherently broader energy spread (compared to conventional accelerators) [21]. While emittance measurements have been successfully performed for LWFA beams in previous studies [22–25], such measurements have not yet been demonstrated for the few-MeV, kHz-rate beams that are particularly relevant for UED.

In this work, we introduce a compact method based on the combination of a permanent magnet solenoid and a dipole magnet, to measure the emittance of few-MeV, kHz repetition-rate LWFA beams for UED, and we validate it through a diffraction experiment. This article is structured as follows: Section II introduces the experimental methods and apparatus. The experimental results are presented in Section III, highlighting the achievement of a low normalized emittance comparable to that of conventional accelerators in the same energy range, and thus meeting UED requirements. Then, Section IV reports on the successful use of the low emittance beams for obtaining clear diffraction images from a single-crystal Silicon sample. Finally, Section V concludes the paper.

II. EXPERIMENTAL METHODS

A. Laser wakefield accelerator

The experimental setup is identical to that described in details in [2], without implementing the differential pumping. The principal information is summarized below. The laser wakefield accelerator is driven by a kHz laser that delivers 4 fs pulses at FWHM with 2.5 mJ on-target energy [26, 27]. The pulses are focused by a 100 mm off-axis parabola down to a 4.5 μm spot at FWHM, reaching a peak intensity in vacuum $I = 1.8 \times 10^{18} \text{ W} \cdot \text{cm}^{-2}$. The laser is focused at a distance of 150 μm from the exit of a continuously flowing supersonic-shocked gas jet with a 180 μm exit diameter [28, 29] with N_2 gas. When performing the emittance measurement, the electron beam charge typically ranged from 200 fC to 1 pC, with a peak energy around 2 MeV. Figure 1 displays a typical spectrum and beam profile from this series of experimental measurements.

B. Emittance measurement apparatus

One of the most widely used technique to measure a beam transverse emittance is the quadrupole scan method (or solenoid scan method) [20, 30]. In this approach, a quadrupole magnet or a solenoid is placed in the beam path, with a screen positioned downstream to monitor the beam profile. By systematically varying the

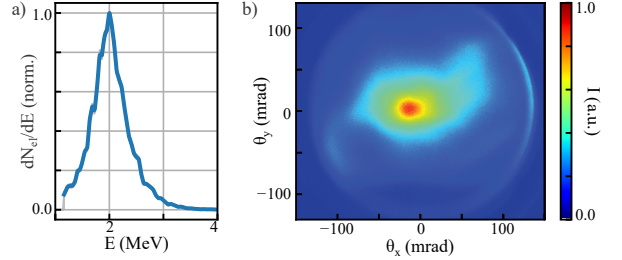


FIG. 1. Typical spectrum (a) and beam profile (b) obtained during the experimental emittance measurement.

magnet's strength and measuring the resulting electron beam size on the screen, one can fit the data to extract the beam's emittance. To refocus the electron beam, we decided to use a solenoid. For a 2.5 MeV electron beam, we typically need a solenoid with an effective magnetic field $B_{eff} = 0.25 \text{ T}$ and a length $L = 40 \text{ mm}$. Traditional current-based solenoids follow the formula:

$$B_{eff} = \frac{\mu_0 N I}{L} \quad (2)$$

where μ_0 is the vacuum permeability, I is the current through the coils, and N is the number of turns in the coil. To achieve the desired magnetic field, we would need $N I = 8 \times 10^3 \text{ A}$. The solenoid must be placed as close as possible to the electron source, under vacuum, and the need for cooling system would make traditional coils extremely impractical. Instead, we use a custom permanent magnet solenoid which offers a more compact and cost-effective alternative.

The experimental setup for emittance measurement is illustrated in Figure 2a. Electrons are accelerated by a laser-plasma accelerator and then pass through a permanent solenoid located at a distance δ from the gas jet, which is the electron source. Here δ is the distance between the gas jet and the solenoid center. A pinhole with diameter $d = 1 \text{ mm}$ is placed before the solenoid in order to reduce the divergence of the beam and therefore improve its emittance. Electrons with a specific energy of 2.5 MeV are focused by the solenoid onto a scintillator screen detector, placed 68.4 cm downstream of the gas jet. The rms transverse size of the beam, σ , is observed on the scintillator for various positions of the solenoid δ . The emittance of the beam is then retrieved by fitting the $\sigma(\delta)$ curve with General Particle Tracker simulations [31] of electron beam trajectory (see Section III C).

Solenoid. The magnet used to focus the electron beam is a custom NdFeB ring magnet with dimensions $20 \times 05 \times 40 \text{ mm}$. The magnetic field is confined using a protective Teflon shell (thickness $\simeq 5 \text{ mm}$) and a soft iron shield (thickness $\simeq 10 \text{ mm}$). The soft iron has a magnetic permeability $\mu_r = 1000$, which allows it to effectively confine magnetic field lines. A schematic of the solenoid mounted in the shell is shown in Figure 2b where the different layers are identified. The solenoid's magnetic

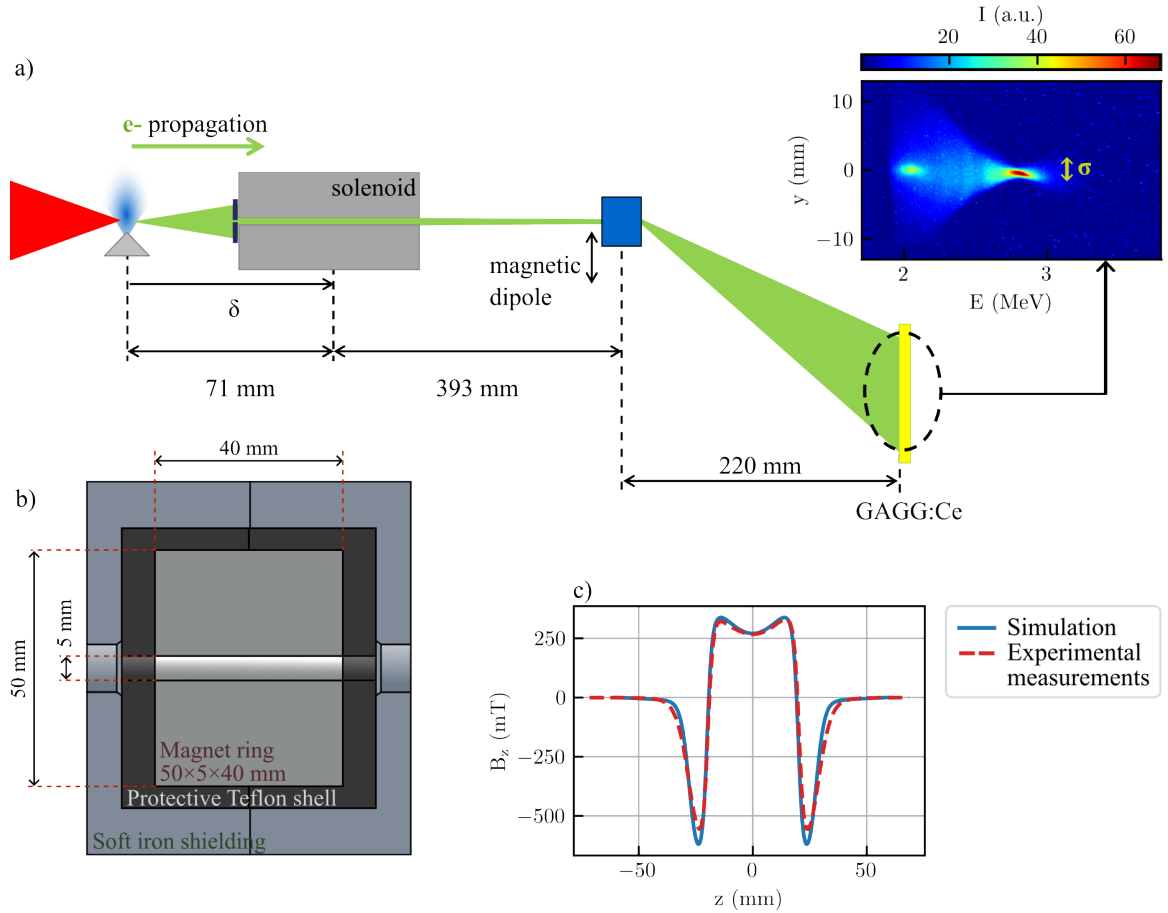


FIG. 2. a) Experimental set up. Electrons, accelerated by laser-wakefield acceleration, pass through the focusing solenoid and the dispersive dipole (which separates them by energy), then hit the scintillator. Without the dipole, the system has a magnification $M \simeq 8$. b) Schematic of the permanent solenoid magnet enclosed in the Teflon shell and soft iron shielding. c) Comparison of the measured on-axis magnetic field and the simulated field using COMSOL.

field was simulated using COMSOL Multiphysics, with the simulations incorporating the detailed geometry of the magnets and shielding, with specified materials to replicate real-world conditions. The simulations were validated against experimental measurements, and Figure 2c compares the measured longitudinal on-axis magnetic field with the simulated results.

Detector. The detector consists of a GAGG:Ce scintillator imaged on a ANDOR Neo 5.5 Megapixel camera. With a read noise as low as 1 e-, this camera introduces minimal uncertainty, equivalent to the signal from a single electron. Particularly low signal levels were anticipated, and this camera was used to enhance the signal-to-noise ratio. The GAGG:Ce scintillator has a high light yield (60 photons/keV, approximately twice that of YAG:Ce), making it more efficient in converting radiation into visible light. To preserve spatial resolution, the scintillator is just 0.1 mm thick, and is mounted on a 1 mm UVFS substrate for structural support. The scintillator is protected by a reflective BaSO_4 layer, coated with a thin 0.06 mm aluminum layer that acts as

a filter for low-energy electrons. Using a Edmund Optics resolution target, the imaging system was characterized to resolve features as small as 15.6 μm (corresponding to $\sigma = 6.6 \mu\text{m}$).

Overcoming the chromaticity problems

The traditional solenoid scan method for emittance measurement is best suited for beams with a narrow energy spectrum [23, 30, 32, 33]. This is because a solenoid has an equivalent focal length f given by:

$$f = \frac{4m_e^2 c^2 (\gamma^2 - 1)}{e^2 B_{\text{eff}}^2 L} \quad (3)$$

where e is the elementary charge, B_{eff} the solenoid's effective magnetic field, and L its length. The Lorentz factor γ is defined as $\gamma = 1 + E/m_e c^2$, where E is the kinetic energy of the electrons. It is clear from this expression that the focal length varies quadratically with electron energy, making the solenoid a highly chromatic device. This chromatic behavior poses a significant experimental challenge: precise focusing requires a well-defined elec-

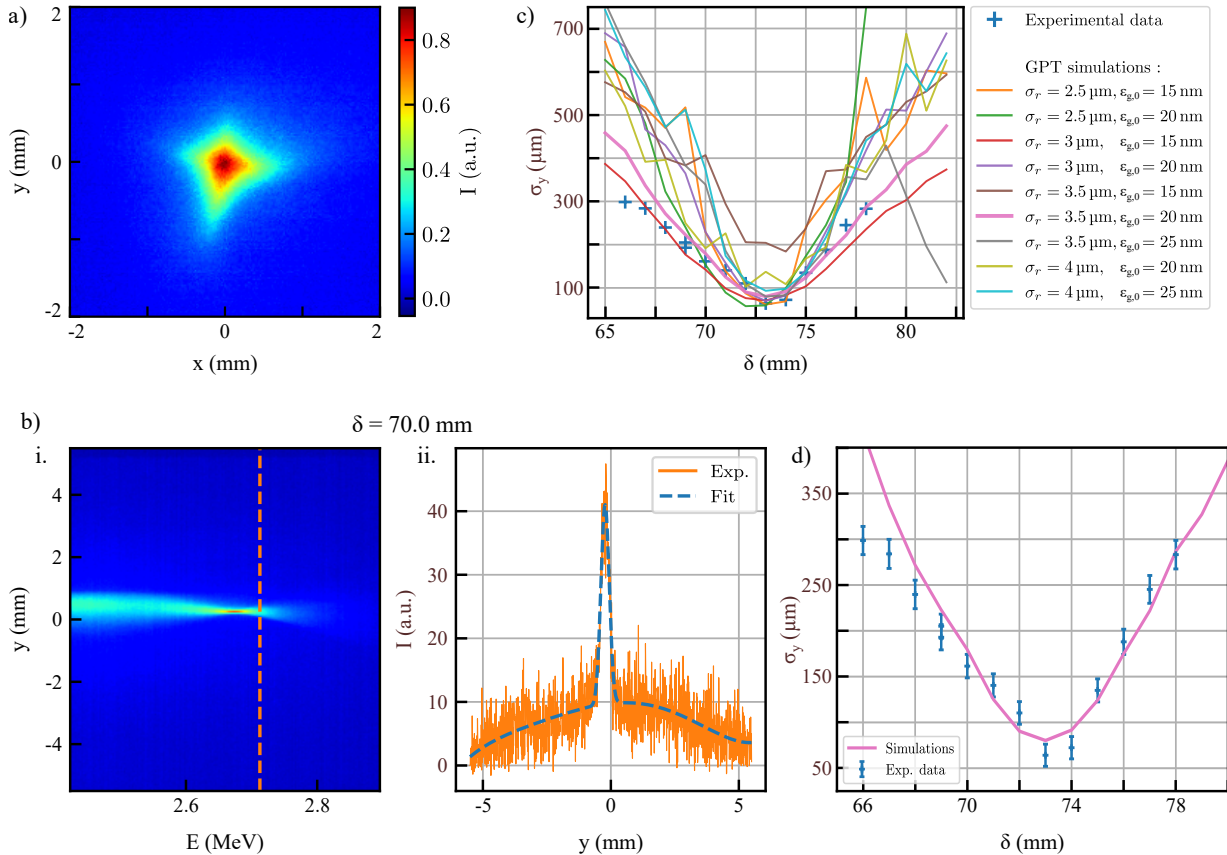


FIG. 3. a) Image of the focal spot with no dispersive dipole. b) Experimental data of the emittance measurement for $\delta = 70.0$ mm. b.i. shows the focused beam registered from the GAGG emission, the orange line indicates the energy $E = 2.7$ MeV selected for analysis and b.ii. shows the cross-section of the beam in the y direction for this energy. c) Plain lines : simulated evolution of the measured cross-section beam size for $E = 2.7$ MeV as a function of the solenoid position for various sets of initial conditions. Blue dots : experimental data for $E = 2.7$ MeV. d) Best fit of the experimental data with simulated data using initial parameters $\sigma_r = 3.5 \mu\text{m}$ and $\epsilon_g = 20 \text{ nm} \cdot \text{rad}$. The error bars account both for the RMS fluctuations of the experimental data and the resolution limits of the imaging system.

tron energy. However, LWFA-accelerated electron beams are rarely mono-energetic, particularly at low energies. For this experimental campaign, the electron beam has a peak energy of 2 MeV with a 0.8 MeV energy spread ($\Delta E/E = 40\%$). The beamline is designed to focus 2.5 MeV electrons onto the scintillator for $\delta = 65$ mm. Consequently, electrons with energies below 2.5 MeV are focused upstream of the scintillator, those with higher energies are focused downstream. This energy spread results in a blurred focal spot on the scintillator, complicating the measurement of the electron beam size.

Facing a similar issue, Weingartner *et al.* proposed to disperse the electrons using a magnetic dipole placed in the electron beam path [25]. The role of the dipole is to separate the energies in the focal plane where the detector is positioned. The dispersed focus then displays a butterfly shape, where the pinch point corresponds to the optimum focused energy, while other energies are out of focus. Figure 2a illustrates our experimental set-up and the butterfly shape at the scintillator position, with the best focus at 2.5 MeV. When varying the position δ of

the solenoid, the width σ of the beam on the detector for a specific energy can be monitored, allowing for more precise measurements.

Dispersive dipole. The dispersive dipole is a set of two NdFeB magnets with dimensions $15 \times 15 \times 4$ mm. These magnets are separated by a distance $d = 18$ mm, generating a magnetic field of approximately 120 mT over 15 mm along the electron beam path. They are encased in a soft iron shielding, to prevent the magnetic field from affecting electron propagation when the dipole is not in the beam path. At 2.5 MeV, the energy resolution is $\delta E/E = 5\%$, ensuring sufficient precision for the emittance measurement.

III. EXPERIMENTAL RESULTS

A. Initial focusing configuration

At first, the electron beam was refocused onto the GAGG scintillator without the dispersive dipole, where elec-

trons travel directly from the gas jet to the GAGG through the solenoid. Figure 3a presents an example of a measured focal spot. Using 20 acquisitions (each with an exposure time $e = 40\text{ ms}$), the FWHM spot size was measured to be $\phi_x = 0.609 \pm 0.023\text{ mm}$ and $\phi_y = 0.615 \pm 0.034\text{ mm}$. The spot size exhibits minimal variation when the solenoid is moved longitudinally, due to the 40% energy spread in the electron beam. This spread results in a blurred focal spot, as electrons of different energies are focused at various positions before and after the screen. Additionally, a cross-shaped pattern was observed, likely due to residual aberrations in the solenoid alignment.

B. Emittance measurement

In the next phase, the dispersive dipole was introduced in the beamline. In this configuration, the electrons first pass through the solenoid and are then dispersed by the dipole. The resulting beam is observed on the GAGG screen where the expected butterfly-shaped distribution is observed. The solenoid's position is scanned from $\delta = 65\text{ mm}$ to $\delta = 78\text{ mm}$, with the corresponding beam profiles being recorded at each position. Figure 3b shows the results for $\delta = 70\text{ mm}$. The i. panel displays the GAGG emission image, representing the spatial electron beam profile. The specific energy $E = 2.7\text{ MeV}$, highlighted by the orange line, is selected for analysis. The beam cross-section at this energy is plotted in the ii. panel. The data are fitted to a function that is the sum of a fifth-degree polynomial and a Gaussian:

$$f(y) = ay^5 + by^4 + cy^3 + dy^2 + ey + f + A \exp\left(-\frac{(y - \mu)^2}{2\sigma^2}\right) \quad (4)$$

The sigma value extracted from the fit is recorded for each solenoid position δ . Figure 3c presents the $\sigma_y(\delta)$ curve for $E = 2.7\text{ MeV}$ with the blue crosses. The beam cross-section at $E = 2.7\text{ MeV}$ decreases to a minimum $\sigma_y = 64.2 \pm 12.1\text{ }\mu\text{m}$ at $\delta = 73\text{ mm}$ before increasing again. The data point at $\delta = 69\text{ mm}$ is duplicated, as a control measurement was taken at this position at the end of the scan. For each solenoid position 20 images were acquired, and with an exposure time of 900 ms (corresponding to 900 shots) for performing statistics. Note that due to the dispersion introduced by the dipole in the x direction, only the beam size in the y direction σ_y is accessible, limiting the measurement to the transverse emittance in this direction. To measure the emittance in the x direction, the dipole must be rotated.

C. General Particle Tracer simulations

To retrieve the emittance from the measured $\sigma(\delta)$ curve while accounting for the real experimental magnetic field, numerical simulations of the electron beam propagation through the beamline were conducted using General Particle Tracer (GPT). GPT is a software package developed by Pulsar Physics to study the 3D dynamics of charged particles in electromagnetic fields [31].

Initialization of the simulations. GPT simulations were performed using 50 to 100,000 macro-particles to model the electron beam, with a total charge $Q = 500\text{ fC}$. Space charge effects are not considered in these simulations. The initial spatial distribution of electrons follows a centered Gaussian distribution, with an adjustable rms width σ_{r_0} . The beam divergence also follows a Gaussian distribution with an rms width $\sigma_{\theta_{xy}} = 25\text{ mrad}$, but it is constrained further in the beamline by a pinhole at the solenoid entrance with diameter $d = 1.0\text{ mm}$, as in the experiment. The beam geometric emittance ϵ_0 is an adjustable parameter. The energy distribution follows a Gaussian distribution centered at $E = 2.7\text{ MeV}$ with an rms energy spread $\sigma_E = 0.5\text{ MeV RMS}$ (negative energies were excluded as they are not physical).

Magnetic elements. The beamline's magnetic field for each element, whether solenoid or dipole, was simulated using either Poisson Superfish (PSF) or COMSOL Multiphysics, and validated against experimental measurements. These simulations incorporated the detailed geometry of the magnets and shielding, with specified materials to closely replicate real-world conditions.

Reproducing the $\sigma(\delta)$ curve. Electrons are generated at $z = 0$, and the screen (scintillator) is positioned at $z = 0.684\text{ m}$ to match experimental conditions. The positions of the electrons are recorded as they crossed the screen. Various initial beam sizes (σ_{r_0}) and initial emittances (ϵ_0) were explored with the simulations. For each set of initial parameters (σ_{r_0} , ϵ_0), multiple simulations were performed by scanning the longitudinal position of the solenoid and the corresponding beam images on the screen were registered, mimicking the experimental procedure. The beam cross-section for the desired energy was extracted, and the $\sigma(\delta)$ curve was plotted, as in the experiments.

D. Fitting experimental data with simulations

Fine-tuned GPT simulations were performed for a range of initial beam sizes and emittances, and the simulated data were compared with the experimental results. The initial beam size σ_r (standard deviation for a Gaussian distribution) was varied from 2.5 to $4\text{ }\mu\text{m}$ in steps of $0.5\text{ }\mu\text{m}$. The initial beam emittance $\epsilon_{g,0}$ was tested from 15 to $25\text{ nm} \cdot \text{rad}$ in $5\text{ nm} \cdot \text{rad}$ increments.

Figure 3c displays the simulated curves overlaid with the experimental data represented by the blue crosses. Among these, the simulation with $\sigma_r = 3.5\text{ }\mu\text{m}$ and

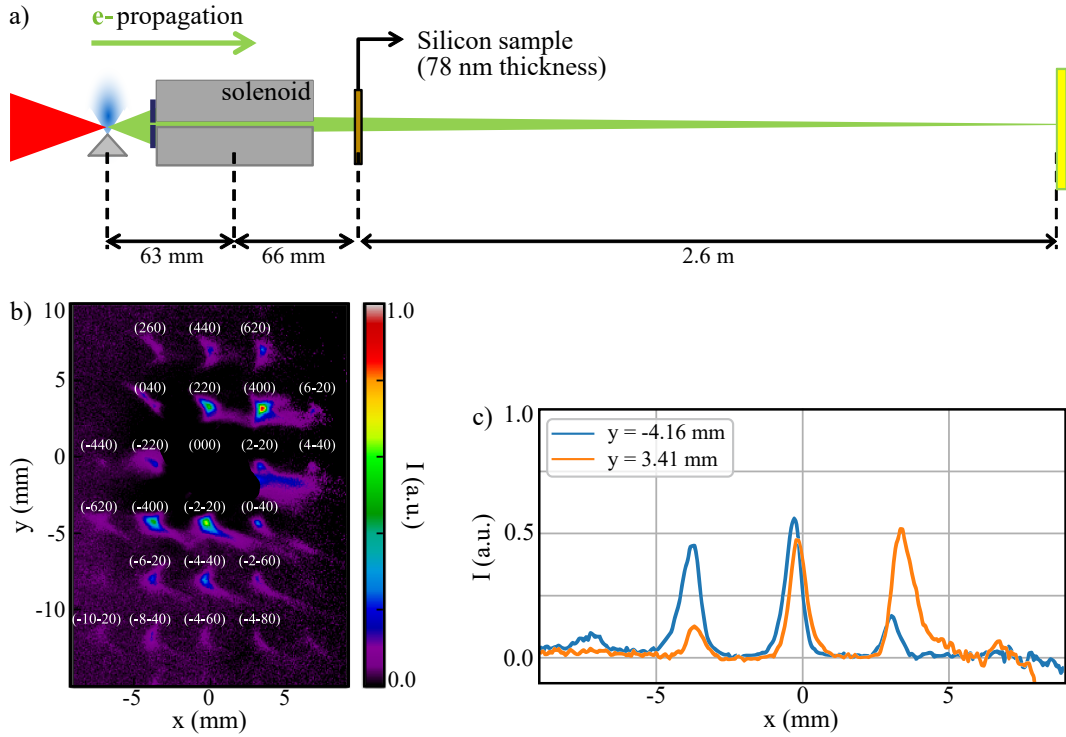


FIG. 4. a) Experimental setup for electron diffraction. Electrons are accelerated via laser-wakefield acceleration and focused by the solenoid onto a scintillator. The silicon sample, on which the electrons diffract, is positioned immediately after the solenoid. The resulting diffraction pattern is observed on the scintillator. b) Diffraction pattern with the sample in place. The image is acquired with a 10 s exposure time, corresponding to 10^4 shots. c) Cross-sectional analysis of the diffraction pattern for $y = 3.41$ mm and $y = -4.16$ mm.

$\epsilon_{g,0} = 20 \text{ nm} \cdot \text{rad}$ provides the best match to the experimental results, as shown in Figure 3d. The error bars for the experimental data account for the optical resolution and the uncertainties in fitting the data to determine the width of the peak. The excellent agreement between simulation and experiment leads to the conclusion that the geometric emittance of the beam is $\epsilon_g = 20 \text{ nm} \cdot \text{rad}$. Given that this was found at the energy $E = 2.7 \text{ MeV}$, the normalized emittance of the beam is $\epsilon_n = 124 \text{ nm} \cdot \text{rad}$. This result was achieved using a spatial filtering of the beam, with 10% of the initial electron beam charge being transmitted.

IV. APPLICATION TO ELECTRON DIFFRACTION

The low transverse emittance measured ($\epsilon_n = 124 \text{ nm} \cdot \text{rad}$) is in the same order of magnitude as $\epsilon_{n,x} \leq 77 \text{ nm} \cdot \text{rad}$ required for resolving diffraction patterns in materials with a lattice parameter $a \simeq 5 \text{ \AA}$ (see Section I). To demonstrate this capability, an electron diffraction experiment was conducted using the available electron beam on a silicon sample.

A. Setting up the diffraction experiment

The layout of the experimental setup for the diffraction experiment is illustrated in Figure 4a.

Sample. A silicon sample consisting of a grid of a single-crystal silicon nanomembrane was used. The nanomembrane has a thickness of 78 nm. Silicon has a diamond cubic lattice structure with a lattice parameter $a = 5.431 \text{ \AA}$ at $T = 300 \text{ K}$. The sample is mounted on a copper holder pierced with holes positioned 31 mm behind the solenoid. The holder is attached to motorized translation stages that allow for alignment along the x and y axes, ensuring that the sample can be precisely aligned with the electron beam.

Detector. To resolve the Bragg peaks on the detector, a separation of $d = 1 \text{ mm}$ between the peaks at the detector position is desired. Using the Bragg formula, $n\lambda_B = 2a \sin \theta_B$ with $n \in \mathbb{Z}$, and assuming a 2.5 MeV electron beam ($\lambda_B = 0.42 \text{ pm}$), the separation angle between the peaks is $\theta_B = 0.38 \text{ mrad}$. To achieve this peak separation of 1 mm, the screen must be positioned 2.6 m behind the sample. In this case the scintillator is a LANEX, and it is positioned 2.67 m behind the solenoid.

B. Experimental results

When the sample was inserted into the beam path, a clear diffraction pattern appeared on the LANEX screen. Figure 4b. shows the resulting diffraction image. The 0-order peak has been attenuated to better visualize the Bragg peaks, which are clearly observable up to the 3rd order. The peaks are not perfectly circular, due to a non-perfect alignment of the solenoid. A cross-sectional analysis of the diffraction pattern observed on the screen is shown in Figure 4c. The intensity profiles along $y = 3.41$ mm and $y = -4.16$ mm are plotted. The distance between two adjacent peaks is approximately 3.5 mm.

Given that the screen is positioned 2.6 m behind the sample and the silicon sample has a known lattice parameter of $d = 5.431$ Å, we can determine the actual wavelength of the electrons using the de Broglie relation:

$$\lambda_B = \frac{h}{m_e c \sqrt{\gamma^2 - 1}} \quad (5)$$

which yields $\lambda_B = 1.46$ pm. This wavelength corresponds to an electron energy of approximately 500 keV. Since we could not measure the electron spectrum and the diffraction pattern simultaneously, and since we optimized the image based on the available signal, it is likely that the electron beam's energy dropped to 500 keV as we attempted to maximize the signal, and that we focused that energy range with the solenoid.

C. Discussion

The reported emittances for various radio-frequency electron guns around the world are displayed in Figure 5 in blue. Our LWFA-based accelerator is highlighted in red. In the few MeV energy range, the best emittance is reported from the SLAC Ultrafast Electron Diffraction (UED) facility, with a value of $\epsilon_{n,SLAC} = 10$ nm · rad. Other existing accelerators in this energy domain have emittances ranging from $\epsilon_n = 60$ nm · rad to $\epsilon_n = 1.9$ μm · rad. Those accelerators deliver electron bunches with charges spanning from 0.2 fC to 30 pC. In light of this, our accelerator's performance is notably competitive, with $\epsilon_n = 124$ nm · rad for a bunch charge $Q = 25 \pm 5$ fC RMS. This demonstrates that kHz LWFA can achieve high beam quality (in terms of emittance), comparable to conventional accelerators.

The subsequent electron diffraction experiment confirmed the potential of our LWFA source for UED studies. With a 25 fC beam, we successfully observed diffraction from a silicon sample, with Bragg peaks clearly visible over several orders, despite a non-ideal focal spot and an electron energy of $E \simeq 500$ keV. However, the non-monoenergetic nature of the beam degrades the temporal resolution due to bunch elongation during propagation.

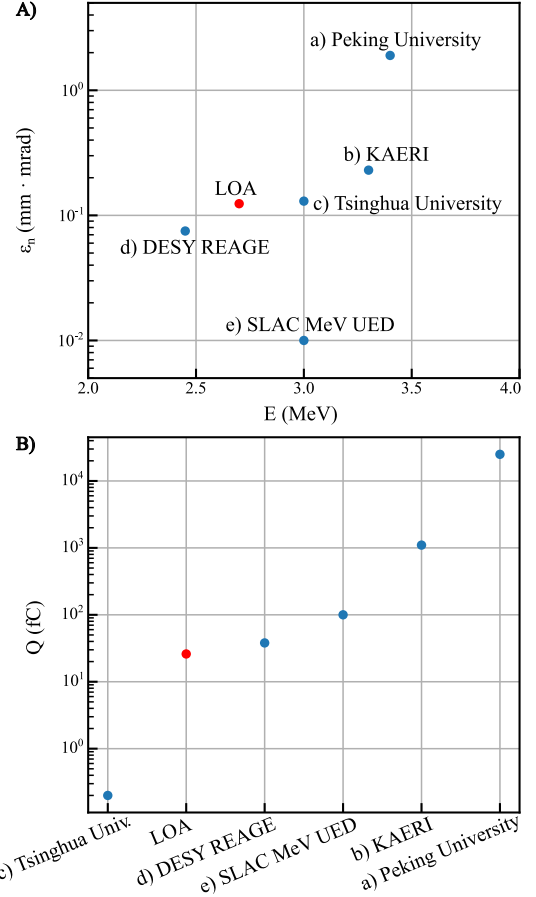


FIG. 5. A) Review of the emittance reported by various conventional accelerator facilities with energies below 10 MeV. a) [34]. b) [32]. c) [35]. d) [36]. e) [37]. B) Corresponding electron beam charges reported.

For a relativistic electron bunch, the duration increase after propagating a distance L is given by [15, 38]:

$$dt = \frac{L}{c} \frac{d\gamma}{\gamma} \frac{1}{\gamma^2} \quad (6)$$

In the current setup, with the sample positioned $L = 129$ mm downstream of the gas jet, an energy $E \simeq 500$ keV and considering $d\gamma/\gamma = 20\%$, the bunch duration broadens by $dt = 22$ ps between the source and the sample. If the diffraction experiment is performed using the best accelerator parameters reported in [2] with $E = 7$ MeV and $\Delta E/E = 10\%$, the broadening would be reduced to $\Delta t \approx 200$ fs. Then to achieve sub-10 fs resolution two approaches can be considered. The first, proposed in [38], involves streaking techniques, which convert temporal information into a spatial diagnostic using the linear energy chirp induced during the drift of the beam in free-space. The second idea is to develop an advanced electron beam transport line to recompress the bunch and minimize the effective energy spread, as demonstrated in [15]. In any case, more work is now needed to tackle the time resolution challenge

with positive prospects for reaching sub-10 fs resolutions [15, 38].

In parallel, it is important to highlight that state-of-the-art RF guns have achieved remarkable performance, producing electron bunches as short as 6 fs RMS with minimal jitter using terahertz streaking [39], or 25 fs RMS bunches with charges up to 0.6 pC and arrival time jitter as low as 7.8 fs [40]: these results set a high benchmark for comparison.

V. CONCLUSION

The primary objective of this study was to produce and characterize an ultra-low emittance beam from a high-repetition rate LWFA and to evaluate the feasibility of conducting electron diffraction experiments in the MeV range using a laser-wakefield accelerated electron beam. The measured normalized transverse emittance, $\epsilon_{n,x} = 124 \text{ nm} \cdot \text{rad}$, is comparable to that of conventional accelerators, demonstrating our accelerator's potential to achieve high beam quality in terms of emittance. Encouraged by these results, we conducted an electron diffraction experiment using the available electron beam. This experiment showcases the significant potential of our kHz LWFA source for electron diffraction studies. With a 26 fC beam, we successfully observed diffraction from a silicon sample, with Bragg peaks clearly visible over several orders despite the non-ideal focal spot. These results highlight the capability of the setup to re-

solve fine structural details.

With further optimization such as improving beam focusing and repeating the experiment with the highest-quality electrons demonstrated with our accelerator, this platform could be used to test pump-probe experiments, paving the way for time-resolved structural studies using LWFA electron beams.

ACKNOWLEDGMENTS

This project has received funding from the European Union's Horizon 2020 research and innovation program under grant agreement JRA PRISE no. 871124 Laserlab-Europe and IFAST under Grant Agreement No 101004730. This project was also funded by the Agence Nationale de la Recherche under Contract No. ANR-20-CE92-0043-01, and benefited from the support of Institut Pierre Lamoure via the "Accélération laser-plasma haute cadence" fund.

We also acknowledge Laserlab-Europe, Grant No. H2020 EC-GA 654148 and the Lithuanian Research Council under Grant agreement No. S-MIP-21-3.

DATA AVAILABILITY STATEMENT

The data that support the findings of this study are available from the corresponding author upon reasonable request.

[1] T. Tajima and J. M. Dawson, Laser electron accelerator, *Physical Review Letters* **43**, 267 (1979).

[2] J. Monzac, S. Smartsev, J. Huijts, L. Rovige, I. A. Andriyash, A. Vernier, V. Tomkus, V. Girdauskas, G. Raciukaitis, M. Mackevičiūtė, V. Stankevič, A. Cavagnaro, J. Kaur, A. Kalouguine, R. Lopez-Martens, and J. Faure, Optical ionization effects in kHz laser wakefield acceleration with few-cycle pulses, *Phys. Rev. Res.* **6**, 043099 (2024).

[3] F. Salehi, M. Le, L. Railing, M. Kolesik, and H. Milchberg, Laser-accelerated, low-divergence 15-MeV quasi-monoenergetic electron bunches at 1 kHz, *Physical Review X* **11**, 021055 (2021).

[4] H. T. Kim, V. B. Pathak, K. Hong Pae, A. Lifschitz, F. Sylla, J. H. Shin, C. Hojbota, S. K. Lee, J. H. Sung, H. W. Lee, E. Guillaume, C. Thaury, K. Nakajima, J. Vieira, L. O. Silva, V. Malka, and C. H. Nam, Stable multi-GeV electron accelerator driven by waveform-controlled PW laser pulses, *Scientific Reports* **7**, 10203 (2017).

[5] K. Oubrerie, A. Leblanc, O. Kononenko, R. Lahaye, I. A. Andriyash, J. Gautier, J.-P. Goddet, L. Martelli, A. Tafzi, K. T. Phuoc, S. Smartsev, and C. Thaury, Controlled acceleration of GeV electron beams in an all-optical plasma waveguide, *Light: Science and Applications* **11**, 180 (2022).

[6] B. Miao, J. Shrock, L. Feder, R. Hollinger, J. Morrison, R. Nedbailo, A. Pickles, H. Song, S. Wang, J. Rocca, and H. Milchberg, Multi-GeV electron bunches from an all-optical laser wakefield accelerator, *Physical Review X* **12**, 031038 (2022).

[7] A. Gonsalves, K. Nakamura, J. Daniels, C. Benedetti, C. Pieronek, T. de Raadt, S. Steinke, J. Bin, S. Bulanov, J. van Tilborg, C. Geddes, C. Schroeder, C. Toth, E. Esarey, K. Swanson, L. Fan-Chiang, G. Bagdasarov, N. Bobrova, V. Gasilov, G. Korn, P. Sasorov, and W. Lee-mans, Petawatt laser guiding and electron beam acceleration to 8 GeV in a laser-heated capillary discharge waveguide, *Physical Review Letters* **122**, 084801 (2019).

[8] C. Aniculaesei, T. Ha, S. Yoffe, L. Labun, S. Milton, E. McCary, M. M. Spinks, H. J. Quevedo, O. Z. Labun, R. Sain, A. Hannasch, R. Zgadzaj, I. Pagano, J. A. Franco-Altamirano, M. L. Ringuette, E. Gaul, S. V. Luedtke, G. Tiwari, B. Ersfeld, E. Brunetti, H. Ruhl, T. Ditmire, S. Bruce, M. E. Donovan, M. C. Downer, D. A. Jaroszynski, and B. M. Hegelich, The acceleration of a high-charge electron bunch to 10 GeV in a 10-cm nanoparticle-assisted wakefield accelerator, *Matter and Radiation at Extremes* **9**, 014001 (2023).

[9] R. J. D. Miller, Femtosecond crystallography with ultrabright electrons and x-rays: Capturing chemistry in action, *Science* **343**, 1108 (2014).

[10] A. H. Zewail and J. M. Thomas, *4D Electron Microscopy* (Imperial College Press, London, 2009).

[11] G. Sciaiani and R. J. D. Miller, Femtosecond electron diffraction: heralding the era of atomically resolved dynamics, *Reports on Progress in Physics* **74**, 096101 (2011).

[12] T. van Oudheusden, P. L. E. M. Pasmans, S. B. van der Geer, M. J. de Loos, M. J. van der Wiel, and O. J. Luiten, Compression of subrelativistic space-charge-dominated electron bunches for single-shot femtosecond electron diffraction, *Phys. Rev. Lett.* **105**, 264801 (2010).

[13] P. Musumeci, J. T. Moody, C. M. Scoby, M. S. Gutierrez, and M. Westfall, Laser-induced melting of a single crystal gold sample by time-resolved ultrafast relativistic electron diffraction, *Appl. Phys. Lett.* **97**, 063502 (2010).

[14] O. Lundh, J. Lim, C. Rechatin, L. Ammoura, A. Ben-Ismaïl, X. Davoine, G. Gallot, J.-P. Goddet, E. Lefebvre, V. Malka, and J. Faure, Few femtosecond, few kiloampere electron bunch produced by a laser-plasma accelerator, *Nature Physics* **7**, 219 (2011).

[15] J. Faure, B. van der Geer, B. Beaurepaire, G. Gallé, A. Vernier, and A. Lifschitz, Concept of a laser-plasma-based electron source for sub-10-fs electron diffraction, *Physical Review Accelerators and Beams* **19**, 021302 (2016).

[16] A. R. Maier, N. M. Delbos, T. Eichner, L. Hübner, S. Jalas, L. Jeppe, S. W. Jolly, M. Kirchen, V. Leroux, P. Messner, M. Schnepp, M. Trunk, P. A. Walker, C. Werle, and P. Winkler, Decoding sources of energy variability in a laser-plasma accelerator, *Physical Review X* **10**, 031039 (2020).

[17] L. Rovige, J. Huijts, I. Andriyash, A. Vernier, V. Tomkus, V. Girdauskas, G. Raciukaitis, J. Dudutis, V. Stankevič, P. Gecys, M. Ouille, Z. Cheng, R. Lopez-Martens, and J. Faure, Demonstration of stable long-term operation of a kilohertz laser-plasma accelerator, *Physical Review Accelerators and Beams* **23**, 093401 (2020).

[18] J. Monzac, S. Smartsev, J. Huijts, L. Rovige, I. A. Andriyash, A. Vernier, V. Tomkus, V. Girdauskas, G. Raciukaitis, M. Mackevičiūtė, V. Stankevič, A. Cavigna, J. Kaur, A. Kalouguine, R. Lopez-Martens, and J. Faure, Differential pumping for kHz operation of a laser wakefield accelerator based on a continuously flowing hydrogen gas jet, *Review of Scientific Instruments* **96**, 043302 (2025).

[19] T. van Oudheusden, E. F. de Jong, S. B. van der Geer, W. P. E. M. O. 't Root, O. J. Luiten, and B. J. Siwick, Electron source concept for single-shot sub-100 fs electron diffraction in the 100 keV range, *Journal of Applied Physics* **102**, 093501 (2007).

[20] K. T. McDonald and D. P. Russell, Methods of emittance measurement, in *Frontiers of Particle Beams; Observation, Diagnosis and Correction*, edited by M. Month and S. Turner (Springer, 1989) pp. 122–132.

[21] A. Cianchi, M. P. Anania, M. Bellaveglia, M. Castellano, E. Chiadroni, M. Ferrario, G. Gatti, B. Marchetti, A. Mostacci, R. Pompili, C. Ronsivalle, A. R. Rossi, and L. Serafini, Challenges in plasma and laser wakefield accelerated beams diagnostic, *Nuclear Instruments and Methods in Physics Research Section A: Accelerators, Spectrometers, Detectors and Associated Equipment* Selected papers from the 2nd International Conference Frontiers in Diagnostic Technologies (ICFDT2), **720**, 153 (2013).

[22] S. Fritzler, E. Lefebvre, V. Malka, F. Burgay, A. E. Danegor, K. Krushelnick, S. P. D. Mangles, Z. Najmudin, J.-P. Rousseau, and B. Walton, Emittance measurements of a laser-wakefield-accelerated electron beam, *Physical Review Letters* **92**, 165006 (2004).

[23] C. M. S. Sears, A. Buck, K. Schmid, J. Mikhailova, F. Krausz, and L. Veisz, Emittance and divergence of laser wakefield accelerated electrons, *Physical Review Special Topics - Accelerators and Beams* **13**, 10.1103/PhysRevSTAB.13.092803 (2010).

[24] E. Brunetti, R. P. Shanks, G. G. Manahan, M. R. Islam, B. Ersfeld, M. P. Anania, S. Cipiccia, R. C. Issac, G. Raj, G. Vieux, G. H. Welsh, S. M. Wiggins, and D. A. Jaroszynski, Low emittance, high brilliance relativistic electron beams from a laser-plasma accelerator, *Physical Review Letters* **105**, 215007 (2010).

[25] R. Weingartner, S. Raith, A. Popp, S. Chou, J. Wenz, K. Khrennikov, M. Heigoldt, A. R. Maier, N. Kajumba, M. Fuchs, B. Zeitler, F. Krausz, S. Karsch, and F. Grüner, Ultralow emittance electron beams from a laser-wakefield accelerator, *Physical Review Special Topics - Accelerators and Beams* **15**, 111302 (2012).

[26] F. Böhle, M. Kretschmar, A. Jullien, M. Kovacs, M. Miranda, R. Romero, H. Crespo, U. Morgner, P. Simon, R. Lopez-Martens, and T. Nagy, Compression of CEP-stable multi-mJ laser pulses down to 4 fs in long hollow fibers, *Laser Physics Letters* **11**, 095401 (2014).

[27] M. Ouillé, A. Vernier, F. Böhle, M. Bocoum, A. Jullien, M. Lozano, J.-P. Rousseau, Z. Cheng, D. Gustas, A. Blumenstein, P. Simon, S. Haessler, J. Faure, T. Nagy, and R. Lopez-Martens, Relativistic-intensity near-single-cycle light waveforms at kHz repetition rate, *Light: Science and Applications* **9**, 47 (2020).

[28] V. Tomkus, V. Girdauskas, J. Dudutis, P. Gečys, V. Stankevič, and G. Raciukaitis, High-density gas capillary nozzles manufactured by hybrid 3d laser machining technique from fused silica, *Optics Express* **26**, 27965 (2018).

[29] A. Marcinkevičius, S. Juodkazis, M. Watanabe, M. Miwa, S. Matsuo, H. Misawa, and J. Nishii, Femtosecond laser-assisted three-dimensional microfabrication in silica, *Optics Letters* **26**, 277 (2001).

[30] B. E. Carlsten, J. C. Goldstein, P. G. O'Shea, and E. J. Pitcher, Measuring emittance of nonthermalized electron beams from photoinjectors, *Nuclear Instruments and Methods in Physics Research Section A: Accelerators, Spectrometers, Detectors and Associated Equipment* **331**, 791 (1993).

[31] General particle tracer, *Pulsar Physics* (accessed in 2024).

[32] S. Setiniyaz, H. W. Kim, I.-H. Baek, J. Nam, M. Chae, B.-H. Han, B. Gudkov, K. H. Jang, S. Park, Y. U. Jeong, S. Miginsky, and N. Vinokurov, Beam characterization at the KAERI UED beamline, *Journal of the Korean Physical Society* **69**, 1019 (2016).

[33] C. A. Lindström, J. Beinortaitė, J. Björklund Svensson, L. Boulton, J. Chappell, S. Diederichs, B. Foster, J. M. Garland, P. González Caminal, G. Loisch, F. Peña, S. Schröder, M. Thévenet, S. Wesch, M. Wing, J. C. Wood, R. D'Arcy, and J. Osterhoff, Emittance preservation in a plasma-wakefield accelerator, *Nature Commun*

nlications **15**, 10.1038/s41467-024-50320-1 (2024).

[34] K. Liu, J.-E. Chen, L. Feng, J. Hao, S. Huang, L. Lin, S. Quan, F. Wang, H. Xie, L. Yang, and F. Zhu, Experimental study on the electron superconducting linac and its application, Proceedings of the 13th Symposium on Accelerator Physics **SAP2017**, 6 pages, 1.460 MB (2018).

[35] R. Li, C. Tang, Y. Du, W. Huang, Q. Du, J. Shi, L. Yan, and X. Wang, Experimental demonstration of high quality MeV ultrafast electron diffraction, Review of Scientific Instruments **80**, 083303 (2009).

[36] DESY REGAE parameters (Accessed March 2025).

[37] MeV-UED specifications | linac coherent light source (Accessed in March 2025).

[38] Z.-H. He, B. Beaurepaire, J. A. Nees, G. Gallé, S. A. Scott, J. R. S. Pérez, M. G. Lagally, K. Krushelnick, A. G. R. Thomas, and J. Faure, Capturing structural dynamics in crystalline silicon using chirped electrons from a laser wakefield accelerator, Scientific Reports **6**, 36224 (2016).

[39] L. Zhao, Z. Wang, C. Lu, R. Wang, C. Hu, P. Wang, J. Qi, T. Jiang, S. Liu, Z. Ma, F. Qi, P. Zhu, Y. Cheng, Z. Shi, Y. Shi, W. Song, X. Zhu, J. Shi, Y. Wang, L. Yan, L. Zhu, D. Xiang, and J. Zhang, Terahertz streaking of few-femtosecond relativistic electron beams, Physical Review X **8**, 021061 (2018).

[40] H. W. Kim, N. A. Vinokurov, I. H. Baek, K. Y. Oang, M. H. Kim, Y. C. Kim, K.-H. Jang, K. Lee, S. H. Park, S. Park, J. Shin, J. Kim, F. Rotermund, S. Cho, T. Feurer, and Y. U. Jeong, Towards jitter-free ultrafast electron diffraction technology, Nature Photonics **14**, 245 (2020).